ADVANCING EARTH AND SPACE SCIENCES

JGR Planets

RESEARCH ARTICLE
10.1029/2025JE009453

Lateral Variations in Lunar Crustal Thickness Inferred From Apollo Seismic and GRAIL Gravity Data

Xiang Zhang[1,2], Taichi Kawamura[1], Mélanie Drilleau[1,3], Philippe Lognonné[1], Samuel Henri[1], Zongbo Xu[1,4], Keisuke Onodera[5], and Thomas Bodin[6]

[1]Université Paris Cité, Institut de physique du globe de Paris, CNRS, Paris, France, [2]Now at Key Laboratory of Deep Petroleum Intelligent Exploration and Development, Institute of Geology and Geophysics, Chinese Academy of Sciences, Beijing, China, [3]Institut Supérieur de l'Aéronautique et de l'Espace ISAE-SUPAERO, Toulouse, France, [4]Now at Norwegian Geotechnical Institute, Oslo, Norway, [5]Institute for Planetary Materials, Okayama University, Tottori, Japan, [6]Instituto de Ciencias del Mar (ICM)–CSIC, Barcelona, Spain

Key Points:

- We used Apollo seismic data beneath impact locations and Apollo stations to determine the local lunar crustal thickness
- The seismic results were quantitatively compared with those obtained from gravity recovery and interior laboratory gravity data
- Integrated gravity and seismic data provide improved insights on the Moho structure of the Moon

Supporting Information:

Supporting Information may be found in the online version of this article.

Correspondence to:

X. Zhang,
zxiang@ipgp.fr

Citation:

Zhang, X., Kawamura, T., Drilleau, M., Lognonné, P., Henri, S., Xu, Z., et al. (2026). Lateral variations in lunar crustal thickness inferred from Apollo seismic and GRAIL gravity data. *Journal of Geophysical Research: Planets*, *131*, e2025JE009453. https://doi.org/10.1029/2025JE009453

Received 17 SEP 2025
Accepted 20 APR 2026

Abstract

The internal structure of the Moon is key to understanding its formation, evolution, and bulk composition. In particular, determining the structure of the crust–mantle interface (Moho), including its lateral variations, is of significant importance, but current knowledge is still insufficient to fully constrain it. To address this, we used seismic wave arrivals from impact events, which yield constraints on the crust at both the impact sites and the Apollo stations, to invert for local crustal thickness. Based on a series of assumed crust and mantle density models, we compared Moho depths inferred from global gravity recovery and interior laboratory gravity data with those from seismic observations. Although the gravity-derived results broadly capture the overall Moho relief, local discrepancies remain, with differences reaching up to 10 km in the vicinity of the Apollo 17 Saturn IVB impact site. These results may reflect regional geological anomalies and highlight the importance of incorporating multiple seismically constrained crustal thickness estimates as anchors in gravity inversions. Using seven seismic anchor points and assuming an upper mantle velocity of $Vp = 7.68$ km/s, an upper mantle density of 3,280 kg/m^3, and a crustal density of 2,693 kg/m^3, we obtain an average lunar crustal thickness of 43.6 ± 1.9 km. The findings also provide valuable guidance for future global 3D modeling of the Moon.

Plain Language Summary

Understanding the Moon's internal structure is important for learning how it formed, evolved, and what it is made of. A key boundary inside the Moon is the crust–mantle interface, known as the Moho, but its depth remains uncertain. In this study, we used seismic waves from impact events to estimate local crustal thickness at both impact sites and Apollo stations. By comparing these seismic estimates with global GRAIL gravity data, we found that gravity broadly captures the Moon's overall crustal structure but can differ locally by up to 10 km. Incorporating multiple seismic measurements as anchors improves the accuracy of gravity-based models. Using seven anchor points and specific assumptions for mantle and crustal properties, we estimate an average lunar crustal thickness of 43.6 ± 1.9 km. These results provide guidance for future global 3-D models of the Moon.

1. Introduction

The structure of the lunar crust–mantle interface (i.e., the Moho), which is a fundamental discontinuity within the Moon's interior, provides important insights into the evolutionary history and compositional characteristics of the lunar crust (Sossi et al., 2025; M. A. Wieczorek et al., 2006). The formation of the lunar crust is understood to result from lighter material floating to the surface of the lunar magma ocean as it cooled and crystallized (e.g., Gaffney et al., 2023). Constraints on the average crustal thickness and its lateral variations are therefore essential for improving our understanding of the initial conditions of lunar formation and evolution (Warren, 2005; M. A. Wieczorek et al., 2013).

The three-dimensional crustal structure of the Moon has mainly been investigated through analysis of global gravity and topography measurements. Data obtained from the Gravity Recovery and Interior Laboratory (GRAIL) and the Lunar Reconnaissance Orbiter (LRO) missions allow us to place constraints on the relative global-scale variations of the lunar crustal thickness (M. A. Wieczorek et al., 2013). Determining the absolute crustal thickness benefits from anchoring points that help better constrain both the average thickness and the densities of the crust and mantle. Seismically constrained crustal thicknesses at distinct locations therefore represent independent observations, which are essential to infer absolute 3D crustal thickness of the Moon.

In previous studies, M. A. Wieczorek et al. (2013) used Moho depths of 30 km (Lognonné et al., 2003) and 38 km (Khan & Mosegaard, 2002), which were mainly representations of crustal thickness beneath Apollo stations 12 and 14, to obtain an average crustal thickness of 34 and 43 km, respectively. Prior to the GRAIL mission, a thicker average lunar crust (about 53 km) was assumed based on the requirement that the minimum crustal thickness be non-negative (Ishihara et al., 2009). In addition to the improved accuracy provided by GRAIL data, this noticeably larger estimate is generally attributed to differences in the selected seismic anchor points and the assumed crustal density. Although GRAIL has greatly enhanced our understanding of the relative lateral variations in the lunar crustal structure, large uncertainties in the seismic anchor points, together with their limited number, continue to challenge our ability to determine absolute crustal thicknesses.

Therefore, to better constrain the lunar crustal thickness, we need to improve the uncertainties on the anchoring points, which can be as large as tens of kilometers (Kim et al., 2025), and to increase their number. Previous investigations using Apollo passive seismic data resulted in different crustal thicknesses below the Apollo 12/14 landing site. The Apollo-era crustal thickness was 60 ± 5 km (Toksöz et al., 1974), more recent reanalyzes of seismic data in the early 2000s suggest a thinner crust of 45 ± 5 km (Khan et al., 2000), 38 ± 3 km (Khan & Mosegaard, 2002), 38 ± 9 km (Kim et al., 2025), and 30 ± 2.5 km (Lognonné et al., 2003). Lognonné et al. (2003) also took into account the S-wave receiver function results from Vinnik et al. (2001), which detected converted phases beneath Apollo station 12, further supporting a thinner crust. Shi et al. (2023) attempted to construct P-wave receiver functions (PRF) using Apollo data, but found that strong coda waves present in lunar seismograms significantly affected the stability of the PRF.

Beyond the Apollo 12/14 site, Chenet et al. (2006) used impact events recorded by the Apollo seismic network to investigate the crustal thickness below different impact sites, taking advantage of the fact that seismic waves generated by impact events, which are seismic sources located at the surface, propagate through the crust, both at the impact site and at the seismic station. This enabled them to constrain crustal thicknesses at locations distant from the Apollo landing sites. They compared the results with a crustal thickness map derived from Lunar Prospector gravity and Clementine topography data, and obtained a mean lunar crustal thickness of 40 ± 5 km, based on the assumption of an upper shallow mantle seismic velocity of $V_p = 7.57$ km/s. However, they did not invert for meteoroid impact locations and crustal velocity simultaneously with crustal thickness. Because crustal thickness may vary significantly for some locations (e.g., close to the edge of a basin, see Neumann et al., 2015), significant uncertainties may remain.

In this study, we build upon and improve the inversion method of Chenet et al. (2006) by inverting for meteoroid impact locations and crustal velocity simultaneously with crustal thickness. We compared our results with the global crustal thickness map derived from the GRAIL gravity data, which provides a higher resolution and accuracy than previous gravity data sets. This will enable a quantitative comparison between seismically detected and gravity-derived estimates of lunar crustal thickness, and provide additional anchoring points outside the Apollo 12/14 site, thereby improving the constraints on the global lunar crustal structure.

2. Apollo Impact Data Set

After the termination of Apollo seismic network operations, the data collected from 1969 to 1977 was fully processed by Nakamura (1983). Prior to this, several groups had been able to identify the major features of the lunar interior using data sets smaller than those currently available (e.g., Nakamura et al., 1974; Toksöz et al., 1974). More recently, the entire Apollo lunar seismic data set has been reanalyzed independently by Nakamura (2003), Lognonné et al. (2003) and Zhao et al. (2015), yielding a new set of P- and S-wave arrival times. A re-compilation of Apollo lunar seismic arrival time data set, including many previous works can be found in Nunn et al. (2020).

However, because of the strong scattering coda present in lunar seismograms, arrival time picks made by different individuals can significantly differ from each other, especially for S-waves which are strongly affected by coda of earlier phases. Readers are referred to for example, Appendix A of Nakamura (2005) and Figure 11 in Nunn et al. (2020) for examples of differences in actual arrival time picks among different investigators. Consequently, it is necessary to re-evaluate these data sets prior to performing an inversion.

The important first step is the selection of seismic events and the reading of arrival times with appropriate error estimates. While the aforementioned studies differ, we can consider their differences as an indicator of data

Table 1
P-Wave Arrival Time Readings for Artificial Impacts

	Lognonné et al., 2003				Nakamura, 1983				New data set			
Event	S12	S14	S15	S16	S12	S14	S15	S16	S12	S14	S15	S16
12 LM	42.4[a] ± 10											
13 SIVB	68.8 ± 1				69.6[b]				69.2 ± 1			
14 SIVB	90.8 ± 1				91.1				90.95 ± 1			
14 LM	46.8 ± 3	44.5 ± 3			51.7	44.5			49.25 ± 10	44.5 ± 1		
15 SIVB	97.0 ± 3	79.7 ± 1			97.9	79.5			97.45 ± 1	79.6 ± 1		
15 LM			64.5 ± 1				59.0				61.75 ± 10	
16 SIVB	31.4 ± 1	47.5 ± 1	150.9 ± 1						31.4 ± 1	47.5 ± 1	150.9 ± 1	
17 SIVB	98.0 ± 1	74.5 ± 1	196.5 ± 3	164.2 ±1	98.3	74.3	193.3	165.4	98.75 ± 1	74.4 ± 1	194.9 ± 10	164.8 ± 1
17 LM												

[a]Arrival times relative to event time (hours and minutes, zero seconds) in Table S1 in Supporting Information S1. [b]There is no clear error bar information in (Nakamura, 1983).

quality. In other words, when the arrival times from multiple studies agree, the data can be regarded as more reliable compared to cases where there are significant discrepancies between the various studies. We selected two independent data sets from Nakamura (1983) and Lognonné et al. (2003), both of which rely on the complete Apollo seismic data set (i.e., the full set of seismic observations compiled after the Apollo seismic stations ceased operation), and have been widely used in many previous studies (e.g., Chenet et al., 2006; Gagnepain-Beyneix et al., 2006; Khan et al., 2006; Khan & Mosegaard, 2002; Lognonné et al., 2003; Nakamura, 1983). For improved consistency, we only selected the arrival times that were consistent between the two data sets.

2.1. Artificial Impacts

During Apollo missions, there were nine artificial impacts caused by the Saturn third stage boosters (SIVB) or the ascent stages of the lunar module (LM) crashed onto the Moon and recorded by the Apollo network. Because of the sequential emplacement of the Apollo stations and the limited amount of energy available, not all artificial impacts were recorded at all stations (Table 1). Moreover, due to the particular signal characteristics of impacts (Section S1 in Supporting Information S1), waveforms exhibit stronger scattering in the crust and S waves are weakly excited, making S waves difficult to identify as they are typically buried in the coda. The data set in Nakamura (1983) contains 6 artificial impact events with 11 arrival time readings (all P-arrivals), while 8 artificial impact events with 17 arrival times (15 P-arrivals, 2 S-arrivals) are included in the Lognonné et al. (2003) data set. We compared the travel time differences between these two data sets, selected the readings for which differences among two data sets are within 10 s, and took their average value as the new arrival time. We assign these new arrival times an error of 1, 3, or 10 s according to the reading time difference within 1, 1−3, or 3−10 s, respectively. We kept the same convention of Lognonné et al. (2003) for error bars, since Nakamura (1983) does not provide clear error bar information.

The Apollo 12 LM impact has a large uncertainty (10 s) and only included in the Lognonné et al. (2003) data set, therefore we exclude this event. Secondly, due to loss of the tracking information during the decent of the Apollo 16 SIVB, location and impact time could not be obtained, Nakamura (1983) did not include this event in his data set. However, this event was recently located by the LRO image (Wagner et al., 2017). Given the high precision in the location (<12 m) and high signal-to-noise ratio of the records, we included this event in our new data set, using the same readings and errors as Lognonné et al. (2003). Finally, the Apollo 17 LM impact was not included in the data sets of either Nakamura (1983) or Lognonné et al. (2003), and we also exclude this event from our new data set. In summary, our new data set consists of 7 artificial impact events, yielding a total of 14 P-arrival times but no S-arrival (Table 1). The locations and impact times of the artificial impact events are well constrained, with the exception of the Apollo 16 S-IVB impact, whose occurrence time is unavailable. Consequently, 13 of the 14 travel times can be used to constrain the internal structural parameters.

2.2. Meteoroid Impacts

We use the same criteria in reading arrival times for meteoroid impacts as for artificial impacts, that is, we select the data for which arrival time differences between Nakamura (1983) and Lognonné et al. (2003) data sets are within 10 s, and take their average. According to the reading time difference within 1, 1−3, or 3−10 s, we assign the data errors of 1, 3 and 10 s, accordingly. Unlike artificial impacts, the locations and origin times of meteoroid impacts are unknown. Therefore, we only select events with at least three independent P-wave arrival time picks from different seismic stations in the new data set, as three arrival times are required to uniquely constrain the impact location (longitude and latitude) and origin time. Note that resolving additional structural information, such as source-side or receiver-side structure, requires more than three arrival times to adequately constrain the additional model parameters.

The Nakamura (1983) data set consist of 18 meteoroid impact events and 63 P-arrival times and 31 S-arrival times. In the Lognonné et al. (2003) data set, there are 19 meteoroid impact events, 70 P-arrival times and 18 S-arrival times. After comparing readings between two data sets, our new data set includes 10 events that are common to both data sets, consisting of 36 P-arrival times and 3 S-arrival times (Table 2 for P waves, Table S2 in Supporting Information S1 for S waves). All seismograms of artificial and meteoroid impact events included in our new data set are shown in Section S3 in Supporting Information S1.

The new data set of artificial and meteoroid impacts will be used in our following work. Although the number of available events is smaller than before, this avoids subjectivity among different studies and provides us with a relatively high-quality data set of events (Figure 1). While our method effectively selects higher-quality data, it may partially underestimate the uncertainty associated with arrival-time picking, because similarly trained seismologists may identify nearly identical arrival times for a given event even in noisy records. As most uncertainties reported here are comparable to or larger than those of Lognonné et al. (2003), we retain this uncertainty level to maintain consistency in error assignment. For a few individual events, the potential effects of adopting uncertainties smaller than those of Lognonné et al. (2003) will be discussed in Section 5.

3. Inversion Methodology

3.1. The Forward Problem

The forward simulation consists of computing synthetic body wave arrival times from a model of the interior structure of the Moon. In the calculation, the Moho relief was taken into account to investigate the local crustal thickness at the impact site and the station (we refer to it as the 3D model hereafter). First, we consider a spherically symmetric lunar surface, without topography. This simplification is intended for computational efficiency and we will later correct for the topography if the difference in elevation between the impact site and the station is greater than 1 km. The travel-time effects associated with smaller elevation differences are negligible relative to arrival-time picking uncertainties. We define a single-layer crustal model whose constant velocity is parameterized using a single value without lateral variations, and the crustal thicknesses at each impact site and Apollo station are parameterized separately. Given that only three S-arrival times were included in our data set, we do not investigate the S-wave velocity structure independently, and fix the V_p/V_s ratio as $\sqrt{3}$ in the single-layer crust (Lognonné et al., 2003; Nakamura, 1983). It is believed that the first few kilometers below the surface consist of highly fractured materials with extremely low seismic velocities (Chenet et al., 2006; Khan & Mosegaard, 2002; Kovach & Watkins, 1973). This low-velocity layer affects the geometry and travel times of seismic rays, causing them to approach near-vertical incidence. To account for the effect of this low-velocity layer in the lunar subsurface, we subtracted 2 s from the P-wave travel times and 4 s from the S-wave travel times, assuming a layer thickness of 1 km and velocities of approximately $Vp = 1$ km/s and $Vs = 0.5$ km/s, corresponding to the two-way travel times for both the receiver-side incident and source-side outgoing rays, then added 1 km to the final crustal thickness results. Below the crust, we used the lunar mantle and core velocity model from Garcia et al. (2019). We evaluated the computational error of this model compared with a two-layer crust model and found it to be small ($\leq$0.1 s) and acceptable, as detailed in the Supplement S4.

Before calculating the synthetic body wave arrival time of the first P- or S-wave arrivals, we determine their ray paths. Given a selected model, we first compute the critical epicentral distance at which the ray begins to reach the mantle. This distance will differ from that obtained using a symmetric crustal model (1D model), as our

Table 2
P-Wave Arrival Time Readings for 27 Meteoroid Impacts

	Lognonné et al., 2003				Nakamura, 1983				New data set			
Event	S12	S14	S15	S16	S12	S14	S15	S16	S12	S14	S15	S16
7105232220						6.6						
7106121051					51.9	59.0						
7110201808					31.9	41.4	15.1					
7201040631	318 ± 10	315 ± 3	215 ± 10									
7205130846	84.9 ± 1	72.1 ± 1	173.5 ± 1	181.0 ± 1	85.2	72.3	174.1	180.3	85.05 ± 1	72.2 ± 1	173.8 ± 1	180.65 ± 1
7207172150	473.7 ± 1	483.0 ± 1	418.2 ± 1	445.8 ± 1	474.0	483.9	419.7	448.8	473.85 ± 1	483.45 ± 1	418.95 ± 3	447.3 ± 3
7207311808	193.4 ± 3	174.7 ± 1	52.6 ± 1		196.1	176.4	52.9	192.0	194.75 ± 3	175.55 ± 3	52.75 ± 1	
7208292258		210 ± 10	132 ± 10	145 ± 10								
7211191824					89.8	94.6	22.1	130.4				
7204231355					109	104	160	41.0				
7309190932					33.8	35.1	110	39.3				
7309262046	295 ± 10	280 ± 10	155 ± 3	192 ± 10								
7312241003	119 ± 3	113 ± 3	250.9 ± 3	190 ± 10								
7404191830	70.9 ± 3	97.0 ± 3	168.3 ± 3	209.2 ± 1								
7407171205	153.4 ± 3	148.7 ± 3	40.6 ± 3	132.1 ± 3								
7411211315	222.9 ± 3	193 ± 3	182.7 ± 10	70.5 ± 1	222.1	201.8	184	71.1	222.5 ± 1	197.4 ± 10	183.35 ± 3	70.8 ± 1
7412150907	95.1 ± 3	66.6 ± 3		128.1 ± 3	93.5	66.2	146.8	128.6	94.3 ± 3	66.4 ± 1		128.35 ± 1
7503052149	236.1 ± 10	225 ± 10		209.7 ± 10								
7504121812	298.1 ± 1	277.8 ± 3	220.6 ± 1	162.1 ± 3	291.6		220.8	164.3	294.85 ± 10		220.7 ± 1	163.2 ± 3
7505040959	360.6 ± 1	376.1 ± 1	436 ± 3	413 ± 1	362.3	374.9	437.7	413.8	361.45 ± 3	375.5 ± 3	436.85 ± 3	413.4 ± 1
7601130711	332.7 ± 3	338.1 ± 10	333.8 ± 3	236 ± 3	333.5	319.4	331.9	242.2	333.1 ± 1		332.85 ± 3	239.1 ± 10
7601251609					48.7		154.4	173.2				
7605161247					191.8		188.4	31.7				
7605280601	163.7 ± 10	126.5 ± 3		169 ± 3								
7611142313	228.6 ± 1	246.9 ± 1	273.8 ± 3	337.7 ± 1	229.1	246.9	274.4	338.2	228.85 ± 1	246.9 ± 1	274.1 ± 1	337.95 ± 1
7704172332	183.7 ± 3	197.8 ± 3	306.4 ± 1	298.2 ± 1	186.4	198.8	309	299.3	185.05 ± 3	198.3 ± 1	307.7 ± 3	298.75 ± 3
7706282222	239.9 ± 3	250 ± 10	344 ± 10	358.5 ± 10								

Note. Event number 7105232220 means the reference impact time 1971/05/23, 22 hr 20 min. Arrival times relative to the reference time (hours and minutes, zero seconds).

calculation is based on a 3D crustal model. We use Snell's law to calculate the critical epicentral distance with the 3D crustal model. As shown in Figure 2, according to Snell's law and the law of Sines, we have the following:

$$\frac{r_0 \sin i}{v_1} = \frac{r_1 \sin i'}{v_1} = \frac{r_1 \sin \beta_1}{v_2} = \frac{r_2 \sin \beta_2}{v_2} = \frac{r_2 \sin \theta'}{v_1} = \frac{r_3 \sin \theta}{v_1} \tag{1}$$

and $\alpha_1 = i' - i$, $\alpha_2 = 180 - \beta_1 - \beta_2$, $\alpha_3 = \theta' - \theta$. If we do not consider topography, then $i = \theta$, $r_0 = r_3$, $r_1 = r_0 - H_i$ and $r_2 = r_0 - H_s$. We can derive the relationship between the epicentral distance and the incident angle:

$$\begin{aligned} \Delta = \alpha_1 + \alpha_2 + \alpha_3 = &\left(\arcsin \frac{r_0 \sin i}{r_1} - i\right) \\ &+ \left(180 - \arcsin \frac{v_2 r_0 \sin i}{v_1 r_1} - \arcsin \frac{v_2 r_0 \sin i}{v_1 r_2}\right) + \left(\arcsin \frac{r_0 \sin i}{r_2} - i\right) \end{aligned} \tag{2}$$

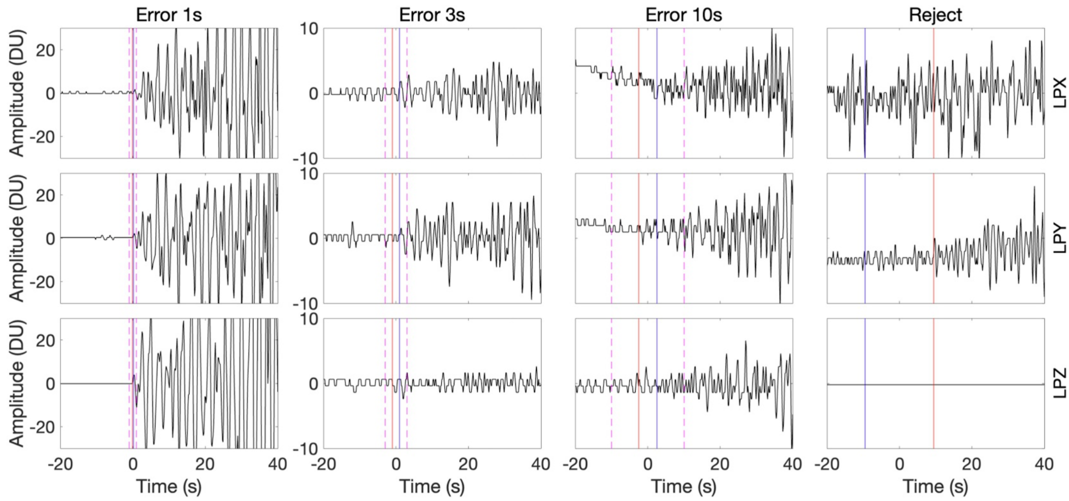

Figure 1. Examples of different quality events. Panels from left to right show impact events 1972-05-13T08:46 (recorded on S12), 1975-04-12T18:12 (S16), Apollo 14 lunar module (S12), and 1976-01-13T07:11 (S14). From top to bottom are shown the horizontal (LPX, LPY) and vertical (LPZ) components, respectively. Time starts from the newly picked P-wave arrival, that is, average value in Nakamura (1983) (blue line) and in Lognonné et al. (2003) (red line). The magenta dotted lines indicate the new error bar for each event.

If we make β_1 or $\beta_2 = 90°$, we can compute the incident angle i, which then allows us to determine the critical distance beyond which the ray begins to propagate into the mantle.

By comparing the epicentral distance between an impact event and a seismic station with the critical distance, we can determine whether the ray propagated through the mantle. We note that the curvature of the lunar Moho

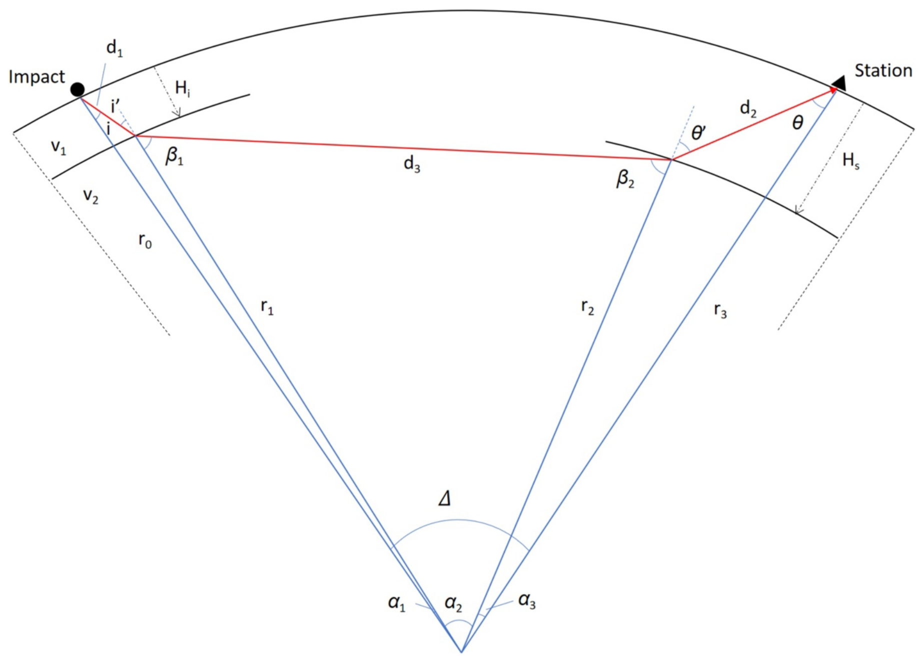

Figure 2. Schematic diagram of the ray path propagating through a lunar model that has different Moho depths at the impact and at the station locations. i represents the take-off angle, while i' denotes the incidence angle at the crust-mantle interface, with β_1 as the corresponding emergence angle. When the ray travels upward, β_2, θ', and θ refer to the incidence angle, emergence angle, and receiving angle, respectively. H_i and H_s represent the crustal thickness beneath the impact site and the station, respectively. d denotes the travel distance of the ray. Δ is the epicentral distance and r represents the radius of the boundary of each layer. v_1 is the P- or S-wave velocity of the crust and v_2 is the P- or S-wave velocity of the mantle.

makes the critical epicentral distance for which the refracted wave can propagate from the mantle always larger than a constant Moho depth model (see Figure S11 in Supporting Information S1 to have a clearer idea of the critical distance variation).

After determining the critical epicentral distance, we compute the P- and S-wave travel time accordingly. For events whose epicentral distances are smaller than the critical distance, we use the following equation to compute the travel time, t, of the direct path from station to impact site within the crust.

$$t = \frac{r_0 \sin\Delta}{\sin((\pi - \Delta)/2)\ v_1}. \tag{3}$$

When the epicentral distance of an event is larger than the critical distance, the calculation of the first-arrival time is carried out in two steps. First we use the Taup toolkit (Crotwell et al., 1999) to compute the 1D model travel times of different crustal thicknesses, then use their average and a compensation item to estimate the target travel time t (Equation 4, Figure S12 in Supporting Information S1).

$$t \ \approx \ (t_1 + t_2)/2 + \frac{\sqrt{(H_i - H_s)^2 + d^2} - d}{v_m}, \tag{4}$$

where t_1 and t_2 are travel times of two 1D models with different crustal thicknesses, v_m is the mean velocity of the mantle (here we consider a value of 7.68 km/s for P-wave, Garcia et al., 2019), $d = (r_1 + r_2) \times \sin\frac{\Delta}{2}$, and Δ is the epicentral distance of the event. The difference between the estimated travel time and the exact travel time is within 0.03 s (Figure S13 in Supporting Information S1), which is significantly smaller than the smallest reading error of arrival times.

After estimating the travel time of the ray traveling through the mantle, in the second step we will calculate the travel time of the direct ray entirely propagating within the crust at the same epicentral distance using Equation 3, then we compare these two travel times and take the smaller one as the first P- or S-wave arrival time.

As mentioned above, relocating meteoroid impacts is important when using them as anchoring points. Therefore, the source locations of the meteoroid impact are also inverted in our investigations. Among the 10 meteoroid impacts in our new data set, two are located on the lunar farside in previous studies (see Garcia et al., 2019). Because we are focusing on the lunar Moho structure, we exclude these farside events and only consider 8 nearside events, which are sensitive to the shallowest part of the velocity model.

3.2. Bayesian Inference

In our study, the inverse problem consists in retrieving the parameters of our lunar model from the observed seismic wave arrival times. However, this problem is ill-posed as different seismic models can result in similar arrival times. To characterize the non-uniqueness of the solution, we cast the inverse problem in a Bayesian framework and use a Markov chain Monte Carlo algorithm to explore the parameter space (Mosegaard & Tarantola, 1995; Tarantola, 2005).

Here we denote by m our model parameter, which consists of the P-wave velocity of the lunar crust, v_p (v_s is deduced from $v_s = v_p/\sqrt{3}$), the crustal thickness below the Apollo stations, H_j, and the crustal thickness below the impact sites, H_i. While the locations are accurately known for artificial impacts (7 events in total), the locations of the 8 meteoroid impacts need to be treated as model parameters, to be determined through inversion. A total of 36 parameters are thus considered and are listed in Table 3.

We define the observed data by the vector **d**, which includes 45 P- and S-arrival times in our data set for both artificial and meteoroid impacts.

In a Bayesian framework, the solution is not a single and unique combination of model parameters that minimizes the fit to observations but rather a full probability distribution in the model space. This posterior solution is proportional to the product of the likelihood and prior distributions (Tarantola, 2005):

Table 3
List of Parameters Inverted in the McMC Algorithm, and the Corresponding Bounds for the Prior Distribution Considered

Description	Quantity	Value/Range
v_p of the crust	1	2–6 km/s
Thickness beneath Apollo station	4	1–100 km
Thickness beneath impact site	15	1–100 km
Latitude of meteoroid impact	8	−90–90°
Longitude of meteoroid impact	8	−90–90°

$$p(\mathbf{m}|\mathbf{d}) \propto p(\mathbf{d}|\mathbf{m})p(\mathbf{m}). \tag{5}$$

The likelihood function $p(\mathbf{d}|\mathbf{m})$ represents the probability of observing the data, given a set of model parameters. This probability distribution follows from a mathematical model of data noise. Assuming Gaussian and independent data errors, the likelihood function can be written as data residuals:

$$p(\mathbf{d}|\mathbf{m}) = \exp\left(-\frac{1}{2}(S_a(\mathbf{d},\mathbf{m}) + S_m(\mathbf{d},\mathbf{m}))\right). \tag{6}$$

For artificial impacts, for which we know the origin time of the event, the misfit function is defined as:

$$S_a(\mathbf{d},\mathbf{m}) = \sum_{i=1}^{N}\sum_{j=1}^{4}\frac{\left(t_{p_{ij}}^{\mathrm{cal}}(\mathbf{m}) - t_{p_{ij}}^{\mathrm{obs}}\right)^2}{\sigma_{p_{ij}}^2}, \tag{7}$$

where i represents different events, j represents different Apollo stations, and σ is the standard deviation of the error associated with each arrival time. t_p^{cal} and t_p^{obs} represent synthetic and observed P-wave travel times, respectively. For meteoroid impacts and Apollo 16 SIVB impact whose origin time is unknown, the misfit function is defined using differential travel times:

$$\begin{aligned} S_m(\mathbf{d},\mathbf{m}) = \sum_{i=1}^{M}\sum_{j=1}^{4}\Bigg(&\frac{\left(\left(t_{p_{ij}}^{\mathrm{cal}}(\mathbf{m}) - t_{refp_i}^{\mathrm{cal}}(\mathbf{m})\right) - \left(t_{p_{ij}}^{\mathrm{obs}} - t_{refp_i}^{\mathrm{obs}}\right)\right)^2}{\left(\sigma_{p_{ij}} + \sigma_{refp_i}\right)^2} \\ &+ \frac{\left(\left(t_{s_{ij}}^{\mathrm{cal}}(\mathbf{m}) - t_{p_{ij}}^{\mathrm{cal}}(\mathbf{m})\right) - \left(t_{s_{ij}}^{\mathrm{obs}} - t_{p_{ij}}^{\mathrm{obs}}\right)\right)^2}{\left(\sigma_{s_{ij}} + \sigma_{p_{ij}}\right)^2}\Bigg), \end{aligned} \tag{8}$$

where t_{refp} is the reference P-wave arrival time recorded by one of the four stations for each event. Specifically, $t_{refp_i}^{\mathrm{obs}}$ represents the observed arrival time of the reference P-wave for the ith event.

3.3. Prior Information

The prior information on the model parameters is given by the prior probability distribution $p(\mathbf{m})$, which represents our current state of knowledge. Here we use a uniform distribution for each parameter within a given range, as summarized in Table 3. The bounds on the prior distributions are defined according to previous studies (Garcia et al., 2019; M. A. Wieczorek et al., 2013).

All meteoroid impacts we use are expected to be located in the nearside, therefore we used for the impact location a range from −90° to 90°. Note that since seismic wave velocities in the mantle are not inverted for, we fixed the mantle velocity model to model M2 from Garcia et al. (2019), which is shown in Figure S14 in Supporting Information S1. Because we only consider nearside events, the velocity model below 1,000 km is not relevant to our results.

3.4. Sampling the Posterior Distribution

To estimate the posterior distribution, we use the Metropolis–Hastings algorithm (Hastings, 1970; Metropolis et al., 1953). The algorithm begins with an initial model and explores the model space through a random walk. At each iteration, a new candidate model is generated by perturbing the current model. The posterior value of the candidate model is then computed, and an acceptance probability is determined based on the ratio of posterior values between the candidate and the current model. The candidate model is either accepted or rejected according to this probability. By repeating this process over many iterations (10^6 iterations in this work), the algorithm produces a sequence of models whose distribution gradually converges to the target posterior distribution (Figure S15 in Supporting Information S1).

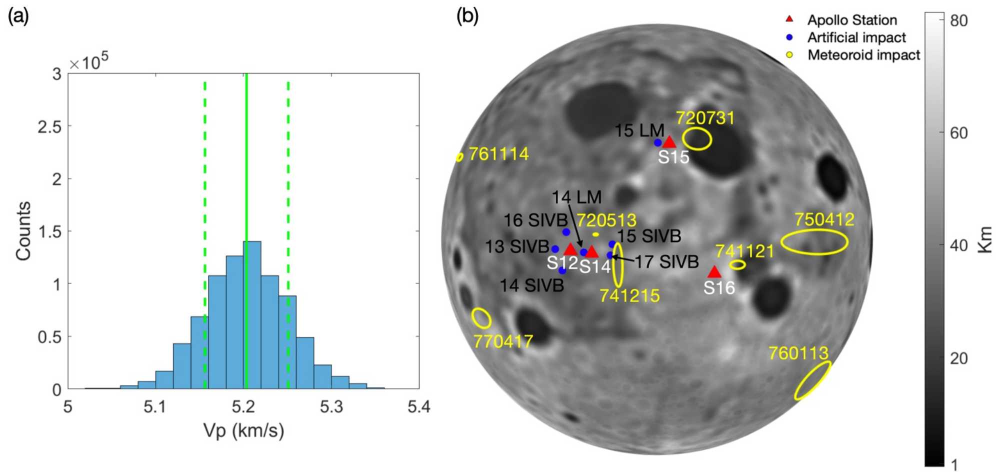

Figure 3. (a) Marginal posterior distribution of P-wave velocity. The green line and dashed lines show the mean and standard deviation. (b) Locations of artificial impact sites (in blue) and inverted location range of meteoroid impacts (in yellow, see Table S6 in Supporting Information S1). Background is the crustal thickness map of the Moon from M. A. Wieczorek et al. (2013), derived from Gravity Recovery and Interior Laboratory gravity data.

4. Inversion Results Using Apollo Seismic Data

Our inversion method was initially validated through tests using synthetic data, which yielded robust and reliable results (see Section S5 in Supporting Information S1 for detailed benchmarking). Following this validation, we applied the method to the actual Apollo seismic data. Figure 3a presents the output ensemble of P-wave velocity models. The P-wave velocity was constrained to a narrow range, with a mean output value of 5.20 km/s and a standard deviation of 0.05 km/s. The corresponding S-wave velocity is 3.00 ± 0.03 km/s.

The inversion results for meteoroid impact locations are shown in Figure 3b. As expected from the synthetic tests we carried out (Section S5 in Supporting Information S1), the uncertainty on the inverted source location strongly depends on the number of arrival picks available, the uncertainties in the arrival time readings, and the geometric relationship with the stations. For example, in the new data set, arrival times were identified at stations S12, S14, and S16, for the event 1974/12/15. Figure 3b shows that these three stations are arranged in an almost linear formation, leading to limited constraints for the event location in the direction perpendicular to the station alignment. Therefore, the uncertainty on latitude is large (± 5.76°), while that on longitude is relatively small (± 1.23°).

The data fits of the arrival times of the 7 artificial events and the relative arrival times of the 8 meteoroid events are shown in Figure 4, which corresponds to a total of 42 P-arrival times and 3 S-arrival times for the 15 impacts. The arrival time errors are represented in red. For artificial impact, the error is the reading error for each event, while for meteoroid impact, the error is the sum of P and P_{ref} errors (see Equation 8). P_{ref} is the reference record for each event which represents as 0 in travel time difference. In general, there is good agreement between observed and computed travel times. Most of the accepted models fit the observational data within the error bars, although some exceed the bounds, especially for meteoroid impacts which have large uncertainties on the locations, such as the meteorite impacts that occurred on 1976/01/13 and 1975/04/12. Artificial impacts represent better fits than meteoroid impacts. This is unsurprising because meteorite impacts involve uncertainties in both time and location, which are further integrated into the definition of the different misfit functions for them (Equations 7 and 8).

The posterior output probability distributions of the lunar crustal thickness for each site are shown in Figure 5. The crust beneath the four Apollo stations is considerably better sampled than that beneath the impact sites, and it is therefore expected to be better constrained than beneath the impact locations. Among the 7 artificial impacts, the pdfs for Apollo 13 SIVB, 14 LM, 15 LM impacts are similar to the a priori distribution. This is due to the short distances between the events and the stations, with epicentral distances smaller than the critical distance. Consequently, the picked first arrivals propagated within the crust without sampling the crust–mantle boundary and therefore provide no constraint on crustal thickness (Figure 3b, Table S7 in Supporting Information S1). Apollo 14 SIVB impact, which was only recorded by Station 12, also only depicts a marginal improvement

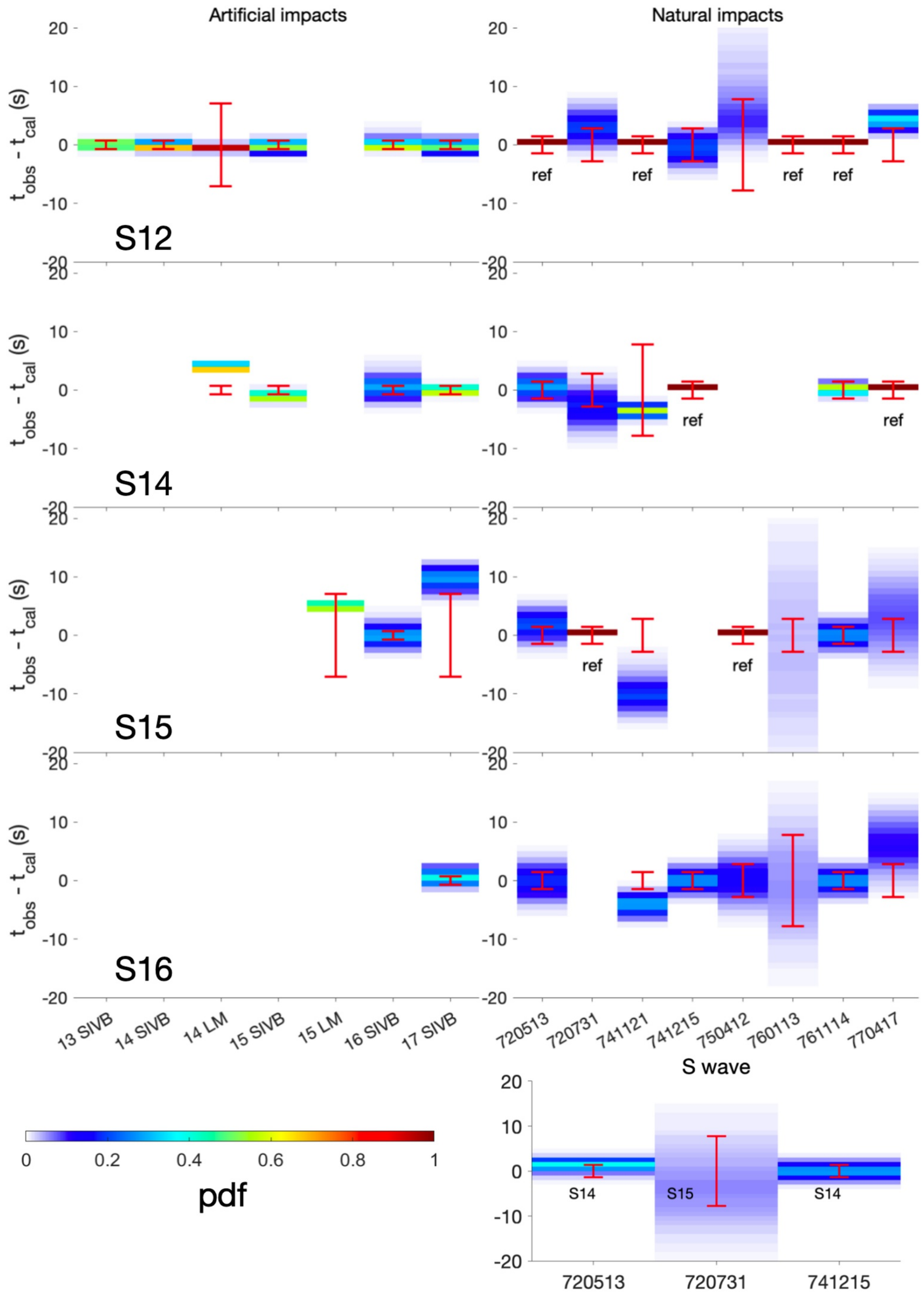

Figure 4. Distribution of the P- and S-wave travel times for each station associated to the posterior distribution in the model space. S-wave travel times are displayed separately in the lower-right corner. Red and blue colors show high and low probabilities, respectively. The red lines represent the error bars, plotted centered at 0 s. For artificial impact events, the error corresponds to the picking uncertainty of each arrival time. For natural impact events, “ref” represents the reference record for each event, selected as the station with the smallest picking uncertainty. The corresponding error bar is given by the sum of the picking uncertainty of each arrival and that of the reference arrival for the event. The reference record of Apollo 16 SIVB is Station 12. Its travel times are plotted in the same way as those of other artificial events for ease of comparison.

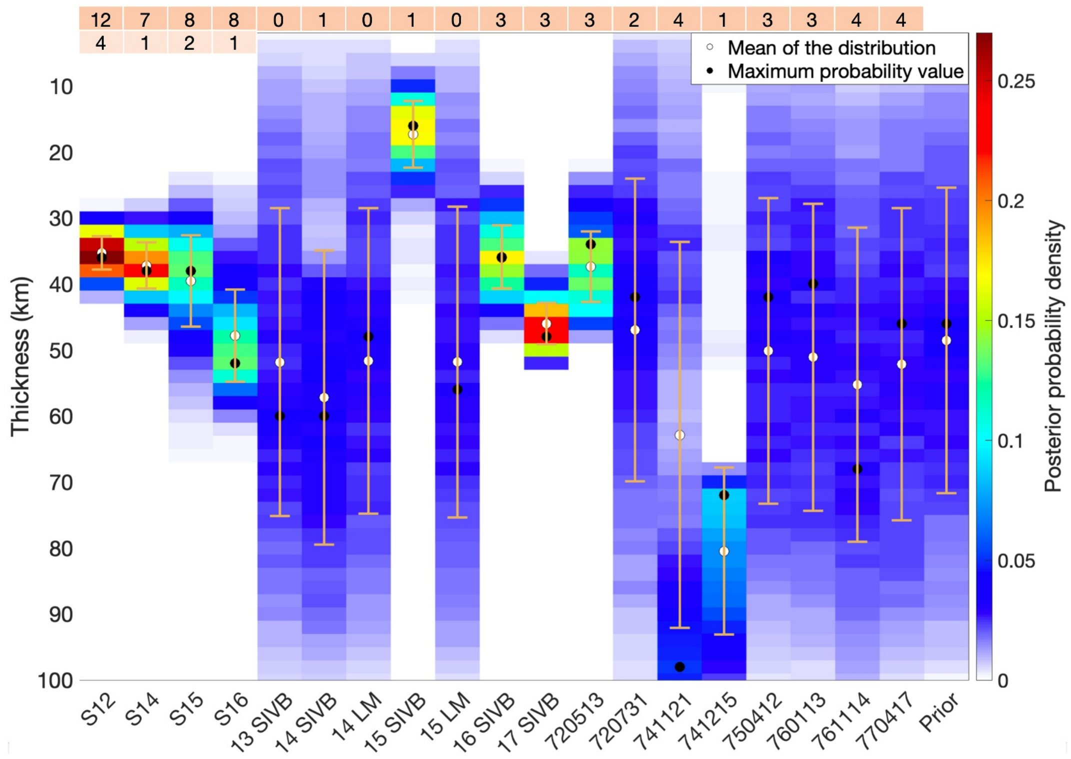

Figure 5. Posterior probability density functions (pdfs) of the crustal thickness at each site (the last one is the prior distribution). Red and blue colors show high and low probabilities, respectively. White dots are mean output values, and the line shows the standard deviation of the posterior values. The black dots represent the maximum probability values at each site. The numbers at the top indicate the sampling frequency at each site, while the smaller numbers below indicate the sampling frequency of artificial impacts recorded by the station. All of these sampling-frequency values correspond to first-arrival ray paths that pass through the mantle and thus provide sampling of the crustal thickness.

relative to the prior distribution. The pdfs for Apollo 15 SIVB, 16 SIVB and 17 SIVB impacts are relatively well constrained.

For the meteoroid impacts, the travel times strongly depend on both crustal thickness and location. Since the location is ill-constrained due to the large uncertainties on the arrival time readings, the trade-off between distance (location) and crustal thickness further compounds the difficulty in constraining the latter(Figures 3b and 5). This is the main reason why crustal thicknesses beneath most meteoroid impacts are largely unconstrained. The crustal thickness beneath the impact on 1972/05/13 is constrained within a narrow range due to the small uncertainty in location, attributed to the high-quality data and the relatively close geometric distances from the stations. This underscores the importance of accurate source location for such inversions. Specifically, larger location errors (>1°) can result in differences of tens of kilometers in crustal thickness.

The event that occurred on 1974/12/15 shows a larger uncertainty in latitude and a significant deviation between its mean value and maximum posterior probability values. Although the crustal thickness is theoretically expected to exhibit a broad distribution across the model space—which is consistent with many other events—its posterior distribution of crustal thickness is narrowly confined (70–100 km). This unusual posterior distribution is likely attributable to the relationship between event epicentral distance and critical distance: when the crustal thickness exceeds 70 km, the critical distance will be larger than the event distances to stations 12 and 14, resulting in travel times that significantly differ from the case where the crustal thickness is thinner than 70 km. Given these statistical and physical inconsistencies, we determined that this event is unreliable and decided to exclude it from the final analysis.

In summary, crustal thickness beneath the four Apollo stations and the impacts Apollo 15 SIVB, Apollo 16 SIVB, Apollo 17 SIVB, and 720513 could be well constrained and will be used for comparison with the gravity-derived 3D crustal thickness map.

10.1029/2025JE009453

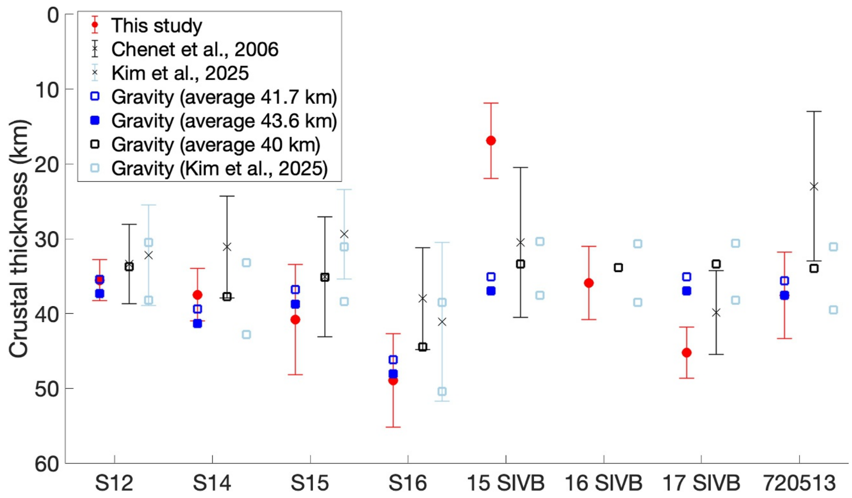

Figure 6. Comparison of lunar crustal thickness derived from seismology and gravity data for different sites. Red and black error bars represent the seismic results from this study and Chenet et al. (2006), respectively. The blue open square represents an average lunar crustal thickness of 41.7 km, inferred from 8 anchoring points. The blue solid square represents an average thickness of 43.6 km, inferred from 7 anchoring points in this study. Black squares show the results from Chenet et al. (2006), who inferred an average lunar crustal thickness of 40 km, excluding event S16 SIVB from their inversion. Light blue error bars denote the seismic-based results from Kim et al. (2025). Light blue squares represent gravity-based results from Kim et al. (2025). The upper and lower squares show the full range of permissible crustal thickness values under different assumptions for mantle and crustal densities (source data from https://doi.org/10.5281/zenodo.15632211).

5. Comparison of Crustal Thickness Derived From Seismic and Gravity Data

We used our derived crustal thicknesses at 4 stations and 4 impact sites as anchoring points and used GRAIL gravity data to determine lateral variations in crustal thickness. The global crustal thickness maps were computed following the same method as in M. A. Wieczorek et al. (2013), and the corresponding software can be found at https://markwieczorek.github.io/ctplanet/index.html. Similarly to our seismic models, the gravity models also consist of a single-layer crust overlying the mantle. We use the GRAIL gravity model GL0420A, truncated beyond degree 310, corresponding to a spatial resolution about 35 km (M. A. Wieczorek et al., 2013). We input different average crustal thicknesses and compute a series of maps from 25 to 58 km, at intervals of 0.1 km, see Section S7 in Supporting Information S1 for details. Then, we compared the crustal thickness obtained from the gravity data with seismic results and evaluated the difference. When the mean crustal thickness is 41.7 km, we obtained the smallest variance (Figure 6). Among these anchoring points, there are two outliers, where the results from the seismic and gravity data do not match within the error bar. One of them is Apollo 15 SIVB, for which only a single data point is available (Figure 3, Table S7 in Supporting Information S1), representing the path that propagates down to the mantle. Therefore, the arrival time reading error can significantly influence the inversion result. We assigned a 1-s uncertainty to this reading according to the reading differences between Nakamura (1983) and Lognonné et al. (2003). However, this reading was assigned a 3-s uncertainty in Lognonné et al. (2003), and two other studies have reported a 5-s difference in this picking (see details in Toksőz et al., 1972; Khan & Mosegaard, 2002). Thus, as discussed in Section 2, this suggests that we may indeed be underestimating the uncertainty associated with this arrival time, and the resulting bias in this pick may contribute to the discrepancy between crustal thickness estimates derived from seismic and gravity data. Consequently, we decided to exclude this event as an anchor to avoid bias.

Apollo 17 SIVB impact was recorded by all four stations and three of the four records have sampled the crust-mantle interface below the impact site and are hence robustly constrained by seismic data (45.23 ± 3.41 km). For the discrepancy between seismology and gravity results (10 km) may indicate local variations in bulk density, potentially caused by localized magmatic intrusions (Besserer et al., 2014). A localized positive density anomaly of 500 ± 100 kg/m^3 could lead to an underestimation of crustal thickness by about 10 km in gravity-derived results (M. A. Wieczorek et al., 2013). Such a density anomaly is consistent with the expected density contrast between basaltic and anorthositic crust. This suggests that, on a local scale, seismic observations could provide higher resolution than gravity data. The resolution of a crustal thickness model does indeed depend on the gravity field resolution at long-wavelengths, but for short-wavelengths, the resolution is dominantly controlled by the input downward continuation filter. The gravity data employed in this study have a precision corresponding to a spatial resolution of roughly 35 km, and we estimate that the spatial resolution of the seismic data is less than 20 km by evaluating the offset between the ray incidence point at the crust–mantle boundary and the surface source point (approximately 0.7°). We have additionally taken into account the recent work by Kim et al. (2025), which provides crustal thickness estimates at a higher spatial resolution than those of M. A. Wieczorek et al. (2013), using spherical harmonic degrees up to 600 (corresponding to a spatial resolution of 10–15 km). Despite this improved resolution, their results also reveal a divergence between gravity- and seismic-based crustal thickness estimates at this site (Figure 6). This provides further evidence for the potential existence of localized density anomalies. However, given the high data quality and the robust seismic constraint, the event itself is considered reliable for anchoring. We therefore decided to keep this event and use in total seven events as anchoring points to re-investigate the global crustal thickness map. The crustal thickness of these events distributed between 35 and 49 km, as listed in Table S8 in Supporting Information S1. The Apollo Station 16 is located in the highlands, making it significantly larger than other sites. Finally, the new global average crustal thickness is 43.6 km, as shown in Figure 6 and Figure S22 in Supporting Information S1. This result falls well within the range reported by Kim et al. (2025) (29−47 km).

6. Discussion

By comparing our results with those of Chenet et al. (2006), we observe that both studies indicate a thicker crust beneath S17 SIVB than inferred from gravity data (Figure 6). There is no doubt that gravity data are sensitive to lateral variations in the depth of the lunar Moho on a global scale (M. A. Wieczorek et al., 2013). However, when investigating the crustal structure beneath a specific location, seismic observations are expected to provide higher resolution than gravity data (better than 20 km). This difference in resolving capability likely explains the discrepancies observed between seismic and gravity-derived crustal thickness estimates at the Apollo 17 SIVB impact site. This also suggests that using a single point as an anchor to calculate a global Moho map could potentially lead to bias. In addition, Below meteoroid impact site 1972/05/13, our results show a better fit to gravity data compared to Chenet et al. (2006), emphasizing the importance of source relocation, and jointly estimating seismic velocity and source location in the inversion analysis.

Here, we used an upper mantle velocity of $V_p = 7.68$ km/s (Garcia et al., 2019), while Chenet et al. (2006) used a velocity of $V_p = 7.57$ km/s based on the model of Gagnepain-Beyneix et al. (2006). This represents a major source of discrepancy in the average crustal thickness reported by the two studies. To independently evaluate the impact of uncertainty in upper mantle velocity Vp, we calculated that a ±0.5% variation (1% variation in total) could result in a difference of approximately 4.5 km in the average lunar crustal thickness. In addition, possible lateral variations in the thickness of the subsurface low-velocity layer and in crustal seismic velocities may also influence the inversion results. Our tests show that varying the low-velocity layer thickness by ±0.5 km (i.e., from 0.5 to 1.5 km) results in a maximum travel-time difference of 1 s. This difference is comparable to the best uncertainty we have today on the arrival time readings, and it could lead to variations of about ±2 km in the estimated crustal thickness. The crustal velocities inferred in this study assume lateral uniformity and therefore do not capture possible lateral variations, which could potentially contribute to the differences observed at some locations between our results and those reported by Kim et al. (2025) (Figure 6).

In our inversions, the assumption of a constant velocity spherical shell is a compromise. Importantly, what we obtain here as a one-layer average crustal velocity is the average apparent velocity of the wave propagating from the surface down to the crust-mantle discontinuity. This may differ from the wave velocity propagating laterally in the crust. This study primarily focuses on the lateral variations in lunar crustal thickness. Similar to the influence of upper mantle velocity, compromises in the crustal velocity model can affect the estimated average crustal thickness, but will not notably affect the relative variations in crustal thickness.

A total of seven anchoring points were used in this study, including four Apollo stations, two artificial impacts, and one meteoroid impact. All these sites are located on the near side. Both highland (station 16) and mare regions (e.g., station 15) were considered. No further site was included, mainly because of uncertainties on the impact locations. Our approach can also be used in future lunar missions that are going to deploy seismometers on the farside of the Moon (Panning et al., 2022; Schmerr et al., 2024; Wang et al., 2024). Furthermore, the approach can benefit from newly lunar impact flash monitoring techniques (Bouley et al., 2012; Ortiz et al., 2006; Sheward et al., 2024) and high-resolution orbit camera which can help us determine the location of impacts.

7. Conclusions and Implications

We improved the method of Chenet et al. (2006), which used the seismic wave arrivals from meteoroid impacts that carry a unique signature of the crust at both impact sites and the Apollo stations, to investigate the local crustal thickness. These results were used in comparison with gravity-derived crustal thickness estimates to constrain and anchor the global lunar crustal thickness model. While we observed general agreement in the Moho relief, significant discrepancies were found at specific locations, which we attribute to the differing resolutions of the seismic and gravity data. Such comparisons were previously limited to qualitative assessments, but the availability of high-precision GRAIL data, combined with our improved seismic inversion methodology, has now made quantitative comparison possible.

Our findings indicate that using seismic results as anchor points to constrain the global average lunar crustal thickness requires careful consideration of both the quality and the number of these anchors. Given that the actual crustal thickness may change rapidly in some areas and the resolution of gravity-derived lunar crustal thickness maps is fundamentally limited by their spatial resolution, relying on a single anchor point can result in substantial errors. An improved strategy involves increasing the number of anchor points while ensuring their quality. It should be noted that uncertainties in the velocities of the upper mantle and lunar crust can affect the results of seismological inversions. If we consider an upper mantle velocity of $V_p = 7.68$ km/s, the anchors obtained in this study indicate an average lunar crustal thickness of 43.6 ± 1.9 km. It should be noted that this does not account for uncertainties in upper-mantle velocities or in the thickness variations of the subsurface low-velocity layer.

While 3D ray tracing has been widely applied in studies of Earth's internal structure (Nolet, 2008), its application to the Moon remains limited due to the current constraints of lunar seismic data. Instead, the global lunar crustal thickness map derived from gravity data serves as a crucial resource for constructing 3D models of the Moon. Validation from seismic data has enhanced our understanding of the potential of model-dependent gravity data in facilitating 3D ray tracing, thereby establishing a foundation for future joint inversion of gravity and seismic data sets. These results will also be valuable for interpreting seismic data acquired by future missions, which are expected to deploy a seismic network on the lunar farside (Panning et al., 2022; Schmerr et al., 2024; Wang et al., 2024), potentially complemented by lunar impact flash monitoring (Lognonné et al., 2025; Sheward et al., 2024, 2025).

Conflict of Interest

The authors declare no conflicts of interest relevant to this study.

Availability Statement

The Apollo seismic data used in this study are archived in the IPGP Research Collection (Zhang et al., 2024). The data set employed to compute the gobal Moho map is available from M. Wieczorek (2012).

Acknowledgments

The authors are grateful to Editor Debra Buczkowski and the two anonymous reviewers for their insightful and constructive comments that have significantly improved the manuscript. We appreciate Mark Wieczorek's help in using GRAIL gravity data to compute the Moho map. XZ was funded by the Key Research Program of the Chinese Academy of Sciences (KGFZD-145-23-15) and the CSC (202104910134). French co-authors acknowledge the support of the French Space Agency CNES and Agence Nationale de la Recherche, ANR (ANR-19-CE31-0008-08). TK, HS, PL acknowledge the support of IdEx Université Paris Cité ANR-18-IDEX-0001. TB has received funding from the Spanish Ministry of Science and Innovation ATR2023-143517/AEI/10.13039/501100011033. Open access publication funding provided by COUPERIN CY26.

References

Besserer, J., Nimmo, F., Wieczorek, M. A., Weber, R. C., Kiefer, W. S., McGovern, P. J., et al. (2014). Grail gravity constraints on the vertical and lateral density structure of the lunar crust. *Geophysical Research Letters*, *41*(16), 5771–5777. https://doi.org/10.1002/2014gl060240

Bouley, S., Baratoux, D., Vaubaillon, J., Mocquet, A., Le Feuvre, M., Colas, F., et al. (2012). Power and duration of impact flashes on the moon: Implication for the cause of radiation. *Icarus*, *218*(1), 115–124. https://doi.org/10.1016/j.icarus.2011.11.028

Chenet, H., Lognonné, P., Wieczorek, M., & Mizutani, H. (2006). Lateral variations of lunar crustal thickness from the Apollo seismic data set. *Earth and Planetary Science Letters*, *243*(1–2), 1–14. https://doi.org/10.1016/j.epsl.2005.12.017

Crotwell, H. P., Owens, T. J., & Ritsema, J. (1999). The taup toolkit: Flexible seismic travel-time and ray-path utilities. *Seismological Research Letters*, *70*(2), 154–160. https://doi.org/10.1785/gssrl.70.2.154

Gaffney, A. M., Gross, J., Borg, L. E., Hanna, K. L. D., Draper, D. S., Dygert, N., et al. (2023). Magmatic evolution I: Initial differentiation of the moon. *Reviews in Mineralogy and Geochemistry*, *89*(1), 103–145. https://doi.org/10.2138/rmg.2023.89.03

Gagnepain-Beyneix, J., Lognonné, P., Chenet, H., Lombardi, D., & Spohn, T. (2006). A seismic model of the lunar mantle and constraints on temperature and mineralogy. *Physics of the Earth and Planetary Interiors*, *159*(3–4), 140–166. https://doi.org/10.1016/j.pepi.2006.05.009

Garcia, R. F., Khan, A., Drilleau, M., Margerin, L., Kawamura, T., Sun, D., et al. (2019). Lunar seismology: An update on interior structure models. *Space Science Reviews*, *215*(8), 50. https://doi.org/10.1007/s11214-019-0613-y

Hastings, W. K. (1970). Monte carlo sampling methods using Markov chains and their applications. *Biometrika*, *57*(1), 97–109. https://doi.org/10.2307/2334940

Ishihara, Y., Goossens, S., Matsumoto, K., Noda, H., Araki, H., Namiki, N., et al. (2009). Crustal thickness of the moon: Implications for farside basin structures. *Geophysical Research Letters*, *36*(19). https://doi.org/10.1029/2009gl039708

Khan, A., Maclennan, J., Taylor, S. R., & Connolly, J. A. (2006). Are the Earth and the moon compositionally alike? Inferences on lunar composition and implications for lunar origin and evolution from geophysical modeling. *Journal of Geophysical Research*, *111*(E5). https://doi.org/10.1029/2005je002608

Khan, A., & Mosegaard, K. (2002). An inquiry into the lunar interior: A nonlinear inversion of the Apollo lunar seismic data. *Journal of Geophysical Research*, *107*(E6), 3-1. https://doi.org/10.1029/2001je001658

Khan, A., Mosegaard, K., & Rasmussen, K. L. (2000). A new seismic velocity model for the moon from a Monte Carlo inversion of the Apollo lunar seismic data. *Geophysical Research Letters*, *27*(11), 1591–1594. https://doi.org/10.1029/1999gl008452

Kim, D., Lekić, V., Wieczorek, M., Schmerr, N., Collins, G., & Panning, M. (2025). A new lunar crustal thickness model constrained by converted seismic waves detected beneath the Apollo seismic network. *Geophysical Research Letters*, *52*(13), e2024GL114506. https://doi.org/10.1029/2024gl114506

Kovach, R. L., & Watkins, J. S. (1973). Apollo 17 seismic profiling: Probing the lunar crust. *Science*, *180*(4090), 1063–1064. https://doi.org/10.1126/science.180.4090.1063

Lognonné, P., Delbo, M., Abe, S., Avdellidou, C., Benna, M., Bickel, V. T., et al. (2025). Lunar impact's seismic and telescopes European network for flash (listen-flash): Integrating an international Earth telescops network and lunar seismic network for multi-messenger impact science and seismology.

Lognonné, P., Gagnepain-Beyneix, J., & Chenet, H. (2003). A new seismic model of the moon: Implications for structure, thermal evolution and formation of the moon. *Earth and Planetary Science Letters*, *211*(1–2), 27–44. https://doi.org/10.1016/s0012-821x(03)00172-9

Metropolis, N., Rosenbluth, A. W., Rosenbluth, M. N., Teller, A. H., & Teller, E. (1953). Equation of state calculations by fast computing machines. *The Journal of Chemical Physics*, *21*(6), 1087–1092. https://doi.org/10.1063/1.1699114

Mosegaard, K., & Tarantola, A. (1995). Monte Carlo sampling of solutions to inverse problems. *Journal of Geophysical Research*, *100*(B7), 12431–12447. https://doi.org/10.1029/94jb03097

Nakamura, Y. (1983). Seismic velocity structure of the lunar mantle. *Journal of Geophysical Research*, *88*(B1), 677–686. https://doi.org/10.1029/jb088ib01p00677

Nakamura, Y. (2003). New identification of deep moonquakes in the Apollo lunar seismic data. *Physics of the Earth and Planetary Interiors*, *139*(3), 197–205. https://doi.org/10.1016/j.pepi.2003.07.017

Nakamura, Y. (2005). Farside deep moonquakes and deep interior of the moon. *Journal of Geophysical Research*, *110*(E1). https://doi.org/10.1029/2004JE002332

Nakamura, Y., Dorman, J., Duennebier, F., Ewing, M., Lammlein, D., & Latham, G. (1974). High-frequency lunar teleseismic events. In *Lunar science conference, 5th, Houston, tex., March 18-22, 1974, proceedings* (Vol. 5, pp. 2883–2890). Pergamon Press.

Neumann, G. A., Zuber, M. T., Wieczorek, M. A., Head, J. W., Baker, D. M., Solomon, S. C., et al. (2015). Lunar impact basins revealed by gravity recovery and interior laboratory measurements. *Science Advances*, *1*(9), e1500852. https://doi.org/10.1126/sciadv.1500852

Nolet, G. (2008). *A breviary of seismic tomography*. Cambridge University Press.

Nunn, C., Garcia, R. F., Nakamura, Y., Marusiak, A. G., Kawamura, T., Sun, D., et al. (2020). Lunar seismology: A data and instrumentation review. *Space Science Reviews*, *216*(5), 89. https://doi.org/10.1007/s11214-020-00709-3

Ortiz, J., Aceituno, F., Quesada, J., Aceituno, J., Fernández, M., Santos-Sanz, P., et al. (2006). Detection of sporadic impact flashes on the moon: Implications for the luminous efficiency of hypervelocity impacts and derived terrestrial impact rates. *Icarus*, *184*(2), 319–326. https://doi.org/10.1016/j.icarus.2006.05.002

Panning, M., Kedar, S., Bowles, N., Bugby, D., Calcutt, S., Cutler, J., et al. (2022). Farside seismic suite (fss): Surviving the lunar night and delivering the first seismic data from the farside of the moon. In *53rd lunar and planetary science conference* (Vol. 2678).1576.

Schmerr, N., Benna, M., McCall, N., Bailey, S., DellaGiustina, D., Bray, V., et al. (2024). The lunar environmental monitoring station: An Artemis 3 deployed instrument. *LPI Contribution*, *3060*, 6010.

Sheward, D., Delbo, M., Avdellidou, C., Cook, A., & Lognonné, P. (2025). Detection of small fresh craters on the moon-linking fresh craters to their lunar impact flash events. *Astronomy & Astrophysics*, *699*, L3. https://doi.org/10.1051/0004-6361/202555481

Sheward, D., Delbo, M., Avdellidou, C., Cook, A., Lognonné, P., Munaibari, E., et al. (2024). Extending lunar impact flash observations into the daytime with short-wave infrared. *Monthly Notices of the Royal Astronomical Society*, *529*(4), 3828–3837. https://doi.org/10.1093/mnras/stad2707

Shi, J., Wang, T., Chen, H., Yang, M., Chen, L., Hui, H., et al. (2023). Differences in scattering properties of the shallow crusts of Earth, Mars, and the moon revealed by p-wave receiver functions. *Journal of Geophysical Research: Planets*, *128*(8), e2022JE007676. https://doi.org/10.1029/2022je007676

Sossi, P. A., Nakajima, M., & Khan, A. (2025). Composition, structure, and origin of the moon. In A. Anbar & D. Weis (Eds.), *Treatise on geochemistry* (479, p. 417). Elsevier. https://doi.org/10.1016/B978-0-323-99762-1.00138-8

Tarantola, A. (2005). *Inverse problem theory and methods for model parameter estimation*. SIAM.

Toksőz, M., Press, F., Anderson, K., Dainty, A., Latham, G., Ewing, M., et al. (1972). Velocity structure and properties of the lunar crust. *The Moon*, *4*(3–4), 490–504. https://doi.org/10.1007/bf00562013

Toksöz, M. N., Dainty, A. M., Solomon, S. C., & Anderson, K. R. (1974). Structure of the moon. *Reviews of Geophysics*, *12*(4), 539–567.

Vinnik, L., Chenet, H., Gagnepain-Beyneix, J., & Lognonne, P. (2001). First seismic receiver functions on the moon. *Geophysical Research Letters*, *28*(15), 3031–3034. https://doi.org/10.1029/2001gl012859

Wagner, R., Nelson, D., Plescia, J., Robinson, M., Speyerer, E., & Mazarico, E. (2017). Coordinates of anthropogenic features on the moon. *Icarus*, *283*, 92–103. https://doi.org/10.1016/j.icarus.2016.05.011

Wang, C., Jia, Y., Xue, C., Lin, Y., Liu, J., Fu, X., et al. (2024). Scientific objectives and payload configuration of the chang'e-7 mission. *National Science Review*, *11*(2), nwad329. https://doi.org/10.1093/nsr/nwad329

Warren, P. H. (2005). New lunar meteorites: Implications for composition of the global lunar surface, lunar crust, and the bulk moon. *Meteoritics & Planetary Science*, *40*(3), 477–506. https://doi.org/10.1111/j.1945-5100.2005.tb00395.x

Wieczorek, M. (2012). Grail crustal thickness archive. *Zenodo*. https://doi.org/10.5281/zenodo.997347

Wieczorek, M. A., Jolliff, B. L., Khan, A., Pritchard, M. E., Weiss, B. P., Williams, J. G., et al. (2006). The constitution and structure of the lunar interior. *Reviews in Mineralogy and Geochemistry*, *60*(1), 221–364. https://doi.org/10.2138/rmg.2006.60.3

Wieczorek, M. A., Neumann, G. A., Nimmo, F., Kiefer, W. S., Taylor, G. J., Melosh, H. J., et al. (2013). The crust of the moon as seen by grail. *Science*, *339*(6120), 671–675. https://doi.org/10.1126/science.1231530

Zhang, X., Lognonné, P., Kawamura, T., Xu, Z., Samuel, H., Sainton, G., et al. (2024). A sub-data set of processed Apollo passive seismic data (impact). *IPGP Research Collection*. https://doi.org/10.18715/IPGP.2024.lsc22f10

Zhao, N., Zhu, P., Zhang, B., & Yuan, Y. (2015). Moonquake relocation. *Earth Science*, 1276. https://doi.org/10.3799/dqkx.2015.107

References From the Supporting Information

Daubar, I. J., McEwen, A. S., Byrne, S., Dundas, C. M., Keska, A. L., Amaya, G. L., et al. (2011). New craters on Mars and the Moon. In *42nd annual lunar and planetary science conference*

Knapmeyer-Endrun, B., & Hammer, C. (2015). Identification of new events in Apollo 16 lunar seismic data by hidden Markov model-based event detection and classification. *Journal of Geophysical Research: Planets*, *120*(10), 1620–1645. https://doi.org/10.1002/2015JE004862

Nakamura, Y., Latham, G. V., Dorman, H. J., & Harris, J. (1981). *Passive seismic experiment, long period event catalog, final version (1969 day 202-1977 day 273, alsep stations 11, 12, 13, 14, 15, and 16) (Tech. Rep.)*. Institute for Geophysics.

Onodera, K. (2024). New views of lunar seismicity brought by analysis of newly discovered moonquakes in Apollo short-period seismic data. *Journal of Geophysical Research: Planets*, *129*(7), e2023JE008153. https://doi.org/10.1029/2023je008153

Plescia, J., Robinson, M., Wagner, R., & Baldridge, R. (2016). Ranger and Apollo sivb spacecraft impact craters. *Planetary and Space Science*, *124*, 15–35. https://doi.org/10.1016/j.pss.2016.01.002

Roncoli, R. B. (2005). Lunar constants and models document. *Jet Propulsion Laboratory*.

Stooke, P. J., & Marcus, M. (2019). Identification of the Apollo 12 lunar module ascent stage impact site on the moon. *Icarus*, *331*, 98–102. https://doi.org/10.1016/j.icarus.2019.05.002

Wieczorek, M. A. (2015). Gravity and topography of the terrestrial planets. *Treatise on geophysics*, *10*, 165–206.

Wieczorek, M. A., & Phillips, R. J. (1998). Potential anomalies on a sphere: Applications to the thickness of the lunar crust. *Journal of Geophysical Research*, *103*(E1), 1715–1724. https://doi.org/10.1029/97je03136